Acta Geochim (2023) 42(1):103–124
https://doi.org/10.1007/s11631-022-00583-6

ORIGINAL ARTICLE

Petrochemical eigenvalues and diagrams for the identification of metamorphic rocks' protolith, taking the host rocks of Dashuigou tellurium deposit in China as an example

Jianzhao Yin[1] · Shoupu Xiang[2] · Yuhong Chao[3] · Yuhan Yin[4] · Hongyun Shi[5]

Received: 29 March 2022 / Revised: 28 October 2022 / Accepted: 3 November 2022 / Published online: 5 December 2022

Abstract The Dashuigou tellurium deposit is the world's only known independent tellurium deposit. By restoring metamorphic rocks' protolith, we seek to understand not only the development and evolution trajectory of the region but also the origin of the relevant deposits. While there are many ways to restore metamorphic rocks' protolith, we take the host metamorphic rocks of Dashuigou tellurium deposit and leverage various petrochemical eigenvalues and related diagrams previously proposed to reveal the deposit's host metamorphic rocks' protolith. The petrochemical eigenvalues include molecular number, Niggli's value, REE parity ratio, CaO/Al_2O_3 ratio, $Fe^{3+}/(Fe^{3+} + Fe^{2+})$ ratio, chondrite-normalized REE value, logarithmic REE value, various REE eigenvalues including scandium, Eu/Sm ratio, total REE amount, light and heavy REEs, δEu, Eu anomaly, Sm/Nd ratio, and silicon isotope $\delta^{30}Si_{NBS-28}‰$, etc. The petrochemical plots include ACMs, 100 mg-c-(al + alk), SiO_2-($Na_2O + K_2O$), (al + fm)-(c + alk) versus Si, (FeO + Fe_2O_3 + TiO)–Al_2O_3–MgO, c-mg, Al_2O_3–($Na_2O + K_2O$), chondrite-normalized REE model, La/Yb-REE, and Sm/Nd ratio, etc. On the basis of these comprehensive analyses, the following conclusions are drawn, starting from the many mantle-derived types of basalt developed in the study area of different geological ages, combined with the previously published research results on the deposit's fluid inclusions and sulfur and lead isotopes. The deposit is formed by mantle degassing in the form of a mantle plume in the late Yanshanian orogeny. The degassed fluids are rich in nano-scale substances including Fe, Te, S, As, Bi, Au, Se, H_2, CO_2, N_2, H_2O, and CH_4, which are enriched by nano-effect, and then rise to a certain part of the crust in the form of mantle plume along the lithospheric fault to form the deposit. The ultimate power for tellurium mineralization was from H_2 flow with high energy, which was produced through radiation from the melted iron of the Earth's outer core. The H_2 flow results in the Earth's degassing, as well as the mantle and crust's uplift.

Keywords Petrochemical diagrams and eigenvalue · Protolith · Metamorphic rock · Independent tellurium deposit · Host rock · The mantle plume

✉ Jianzhao Yin
jzyin7@jlu.edu.cn

Shoupu Xiang
shoupux@163.com

Yuhong Chao
435975944@qq.com

Yuhan Yin
yinyh1207@foxmail.com

Hongyun Shi
hongyunshi@yahoo.com

[1] College of Earth Sciences, Jilin University, 2199 Jianshe Street, Changchun 130061, China

[2] Silvercorp Metals Inc, Suite 601-Building 1, China View Mansion, #A2 East GongTi Road, Chaoyang District, , Beijing 100027, China

[3] Engineering Geology Brigade of Jiangxi Bureau of Geology, 658 Jiefangxilu Road, Nanchang 330002, Jiangxi Province,, China

[4] Xuchang Electrical Vocational College, Xuchang 461000, China

[5] Orient Resources Ltd, 9280 Kirkmond Crescent, Richmond, B.C V7E 1M8, Canada

1 Introduction

As the only identified independent tellurium deposit in the world (Yin 1996a, b), the Dashuigou tellurium deposit has aroused widespread curiosity from domestic geologists in China since its discovery in 1992. There exist divergent opinions on the origin of both the ore-forming elements and the Dashuigou tellurium deposit itself (Cao et al. 1994, 1995; Luo et al. 1994, 1996; Chen et al. 1994a, b, 1996; Yin 1996a, b; Yin and Shi 2019; Wang et al. 2000).

Yin (1996a, b), Yin and Shi (2019), one of the authors of this paper, proposed that scattered elements including tellurium and bismuth originated from the deep Earth, mainly through the mantle's degassing in the form of a mantle plume or hot spot, and enriched through nano-effect.

This paper attempts to further prove the close relationship between the upper mantle and the origin of the deposit, that is, the causal relationship between its formation and mantle degassing in the form of a mantle plume, from the perspective of the protolith's origin of the deposit's metamorphic host rocks. More importantly, this paper focuses on various petrochemical diagrams and numerous eigenvalues for the protolith's restoration of the metamorphic rocks. The authors hope that this article's publication will aid in the efforts of others who are engaged in similar metamorphic rock research.

2 Regional geology and geophysics

2.1 General

Nestling in the convergence between the Indian, Eurasian, and Pacific Plates, the Dashuigou tellurium deposit is located in the transitional belt between the Yangtze Platform and Songpan-Ganzi folded belt (Fig. 1). Geophysical data indicates that the upper mantle below the region uplifts obviously (Luo et al. 1994, 1996; Yin 1996a). The area possesses high heat flow. There is also a low-velocity and low-resistivity zone in the middle crust that is interpreted as a decollement. It is also a gravity gradient zone that controls not only the production and development of earthquakes and tectonomagmatic events, but also the distribution of a series of mineral deposits. The crust-mantle structures and properties in the region are the result of tectogenesis through various geological times. It implies the turning boundary of the Earth's crust's thickness.

In a word, the region exhibits geophysical characteristics of high velocity, high density, high resistance, high geothermal flow, and high magnetism.

It is believed that there exists an abnormal mantle under the crust in the region, which has properties of geosyncline, platform, and its own special characteristics. The belt is a geo-tectonically active zone with very complicated igneous rock structures. In summary, this region is both geologically active and a very important south-north trending tectonomagmatic-mineral belt (Luo et al. 1996; Yin 1996a).

2.2 Strata

Generally, the strata, which are low-grade metamorphic rocks of the Silurian, Devonian, and Permian systems and middle-lower Triassic series, igneous rocks, and structures trend south-northward. A large amount of Archaean metamorphic rocks of the Kangding Group emerge to the southeast of the deposit (Table 1, Yin 1996a).

2.3 Igneous rock

The well-developed igneous rocks in the region include ultrabasic, basic, neutral, acid, and alkaline produced during different geological times. Large neutral, acid, and alkaline intrusive bodies exist beyond 10 km of the deposit (Fig. 1). These intrusive rocks are briefly described as follows (Yin 1996a):

2.3.1 The Archean-Early Proterozoic Jiziping-Caluo granite

Located 10 km east of the study area, comprised of mainly quartz diorite and diorite extending north–south, covering an area of 55 km^2. These intrusive rocks are alkali-poor, sodium-rich, low-potassium, SiO_2 supersaturated-strongly supersaturated, with medium–low abundance ΣREE, rich ΣLREE, weak or insignificant negative europium anomaly, initial Sr^{87}/Sr^{86} ratio of 0.704, and $\delta^{18}O_{SNOW}‰$ of 6.00–9.11. The diagenetic material mainly comes from the upper mantle, and the original silico-alumina crustal material is mixed to varying degrees locally (Yin 1996a).

2.3.2 The Late Proterozoic Xiaoshui granite

Widely exposed in the eastern portion of the study area and is distributed in a north–south direction across a huge area of 950 km^2. It is primarily ordinary granite, with some flesh-red alkaline granite, which has different lithofacies and is most widely distributed in transition lithofacies. Its isotopic age is 6.64–7.24 Ma (Yin 1996a). The average chemical compositions of the ordinary granite and feldspar granite in this granite batholith are 74.25% and 75.53% for SiO_2, 12.81% and 12.19% for Al_2O_3, and 4.44% and 4.06% for Na_2O (Yin 1996a), which are consistent with the results

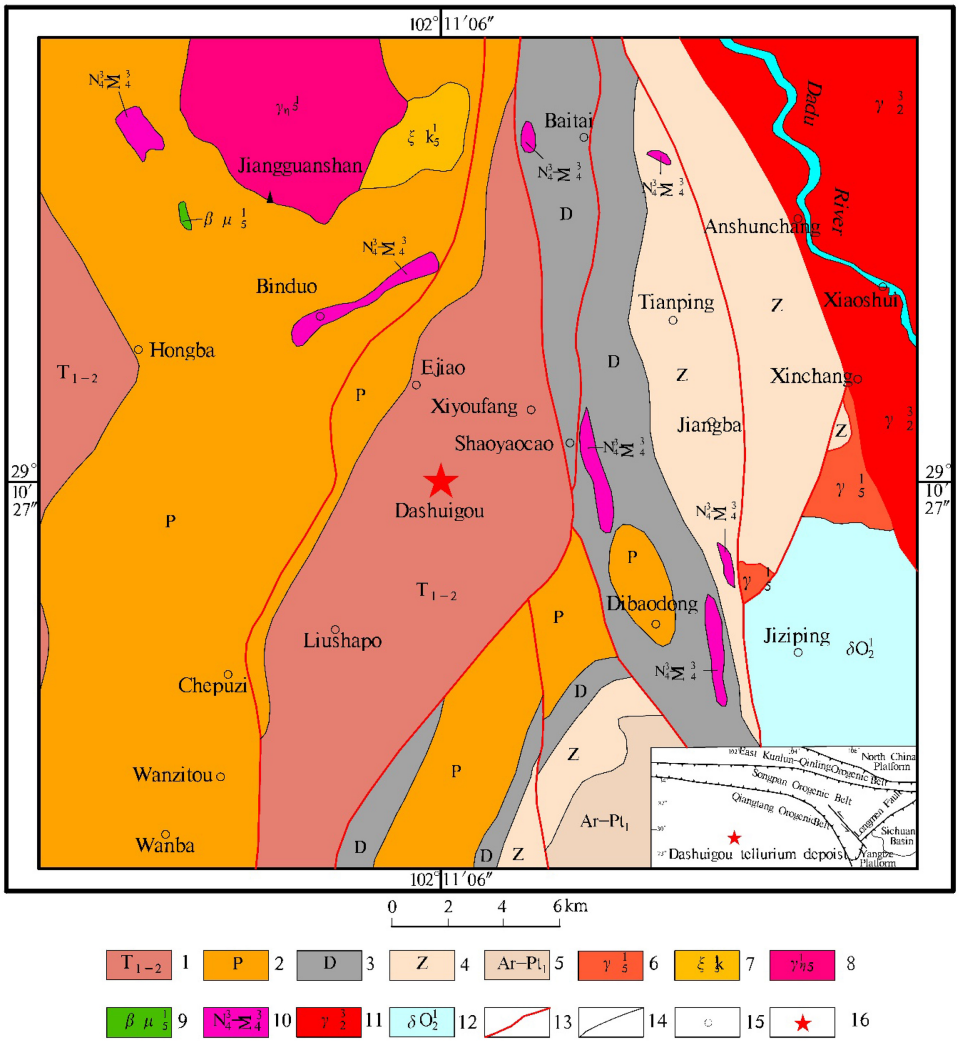

Fig. 1 Regional geology (Yin 1996a). 1. The Lower and Middle Triassic metamorphic rocks; 2. The Permian metamorphic rocks; 3. The Devonian metamorphic rocks; 4. Metamorphic rocks of the Sinian system; 5. The metamorphic base complex of the Archean Kangding group; 6. Plutonic granite of the Indosinian orogeny; 7. Plutonic alkaline syenite of the Indosinian orogeny; 8. Plutonic monzonitic granite of the Indosinian orogeny; 9. Hypabyssal sillite of the Indosinian orogeny; 10. The Late Hercynian basic-ultrabasic rocks; 11. The Late Proterozoic plutonic granite; 12. The Early Proterozoic-Archean plutonic quartz diorite; 13. The deep and large fault; 14. The geological boundary; 15. Village and/or town; 16. The tellurium deposit

of this study (Table 2). The batholith is a typical orogenic product. The formation depths of ordinary granite and potassium feldspar granite are 3.0–6.5 km and 2.0–6.0 km, respectively (Yin 1996a). Iron, tin, and tungsten ore bodies are produced in some parts of the batholith, and Ta, Nb, and Y mineralization occur in the alkaline granites.

Potassium feldspar granite and ordinary granite contain 3.22×10^{-6} and 9.12×10^{-6} scandium respectively (Table 3), which is slightly higher than the average abundance of scandium in acid rocks (Table 4). Their Eu/Sm ratios are 0.017 and 0.103 respectively (Table 5), which are lower than the average values for granite (Table 6). Their REE parity ratios, namely EREE/OREE values, are 2.609 and 2.403 respectively (Table 5), which are lower than the average values for granite, but close to that of the sedimentary rocks in northern Guangxi, the European Paleozoic shale, and the Russian platform shale (Table 7, Hu et al. 1990), showing the origin of the Earth's crust.

In general, these two types of granites have high ΣREE (Table 5), in addition to moderate enrichment of LREE and strong depletion of Eu, both of which show a seagull-like curve gently sloping to the right (Fig. 2), indicating that the two different granites from the same batholith are of the same origin.

The ordinary granite's $\delta^{18}O_{SMOW}$ and initial Sr^{87}/Sr^{86} ratio are respectively 11.89‰ and 0.718, indicating that the diagenetic material originates from the crust and belongs to S-type granite. The $\delta^{30}Si_{NBS}$‰ of ordinary granite and potassium feldspar granite are −0.1 and 0.2 respectively (Table 8 & Fig. 3), which is within the average range of $\delta^{30}Si_{NBS}$‰ variation for granite. According to Ding et al. (1994), the world's existing granites' $\delta^{30}Si_{NBS}$‰ are between $-0.4 \sim 0.4$, with a peak value of −0.1 and an average value of −0.12.

Table 1 Summary of the regional stratigraphic sequence, sedimentary formation, and lithology in the study area

Geological time			Tectonic layer	Sedimentary formation and lithology	Note
Era	Code	System			
Cenozoic	Q	Quaternary	Himalayan tectonic layer	The upper part is the alluvial layer, the middle part is the glacial layer, and the lower part is the mixed sedimentary layer of alluvial, slope and glacial deposits	Unconformity Contact
Mesozoic	T_{1-2}	Lower-Middle Triassic	Cover	Marine carbonate and basic volcanic rock sedimentary formations, which have been metamorphosed to marble, slate and schist	Conformity or fault contact
Paleozoic	P	Permian		The upper part is formed by clastic rocks, marine carbonate and basic volcanic rocks, and the lower part is formed by marine carbonate; it has been metamorphosed into slate, marble and schist respectively	Conformity or fault contact
	D	Devonian		The upper part is formed by marine carbonate, and the lower part is formed by clastic rock and marine carbonate, which has been metamorphosed to marble and slate, etc	Fault or/and pseudoconformity contacts
Proterozoic	Z	Sinian		Formation of marine carbonate and clastic rocks, which have been metamorphosed to marble and slate, etc	
	Pt_1				
Archean	Ar	Kangding Group metamorphic complex	Crystalline basement	Basic, medium and acid volcanic rock formations and flysch-like formations; have been subjected to regional dynamic metamorphism, becoming high greenschist facies and amphibole facies metamorphic rocks	Angular unconformity and fault contact

Table 2 Chemical compositions of the Late Proterozoic Xiaoshui and Late Paleozoic Xinchang granites (%)

Series #	Sample ID	Sample type	SiO_2	Al_2O_3	TiO_2	Fe_2O_3	FeO	CaO	MgO	K_2O
9	SL-01	Granite (γ_5^1)	65.78	14.62	0.43	1.46	3.18	4.76	2.26	1.86
10	SL-26	K-granite (γ_{k2}^3)	75.92	11.66	0.12	0.36	1.96	0.45	0.16	5.49
11	SL-22	Granite (γ_2^3)	71.34	13.72	0.30	1.52	1.48	1.52	0.36	4.74
Series #	Sample ID	Sample type	Na_2O	MnO	P_2O_5	CO_2	H_2O^+	H_2O^-	Organic carbon	Total
9	SL-01	Granite (γ_5^1)	3.55	0.07	0.08	0.29	0.72	0.12	0.00	99.29
10	SL-26	K-granite (γ_{k2}^3)	2.78	0.03	0.00	0.49	0.54	0.32	0.29	100.54
11	SL-22	Granite (γ_2^3)	3.59	0.06	0.05	0.21	0.62	0.20	0.09	99.80

Please refer to Table 3 for the sampling location

2.3.3 Late Paleozoic basic-ultrabasic intrusive rocks

There are seven basic-ultrabasic intrusive rocks, which are exposed in the form of rock beds, sheets, and dykes in the eastern and northwestern parts of the study area. The exposed areas are less than 1 km^2 each and most trend north–south with certain differentiation characteristics: the core is pure peridotite, and outwards are pyrolite, peridotite, olivine pyroxenolite, pyroxenite, and gabbro, where peridotite is more common. Tremolite and asbestos are often enriched in certain kinds of intrusive rocks, magnetite is enriched in other intrusive rocks, and some intrusive rocks have copper and nickel mineralization. Among them, there are two relatively large rock stocks, namely the Binduo and the Shaoyaocao stocks. The Binduo stock is an iron-bearing ultrabasic rock, rich in asbestos in the northeast and magnetite in the southwest, accompanied by a small amount of pyrrhotite, nickel, and cobalt. Tremolite and asbestos were found within the Shaoyaocao stock. Geological and geochemical data show that these basic-ultrabasic intrusive rocks originated in the upper mantle, which is directly related to the Xiaojinhe lithospheric fault zone (Yin 1996a).

2.3.4 Mesozoic neutral, acidic and alkaline intrusive rocks

Includes Jiangguanshan alkaline syenite, Jiangguanshan quartz diorite, and Xinchang granite. Among them, the

Table 3 REE compositions of various rocks and minerals in the study area (%)

Series #	Sample ID	Sample type	Sample site		Sample age
1	SL-05	Slate	At the Liushapo		Early and Middle Triassic (T_{1-2})
2	SD-56	Slate	In ore body I-10's hanging wall		
3	SL-11	Quartz from a tourmaline-bearing quartz vein	At the Liushapo		
4	SL-18	Striped (banded) marble	Near the Tizigou		
5	SD-49	Striped (banded) marble	At the #4 shaft's portal		
6	SD-69	Coarse-grained marble	At Dashuigou ditch's bottom		
7	SL-03	Slate	At the Heba	Late Permian (P_2)	Upper black rock section (P_2^4)
8	SL-10	Metamorphosed basalt	Near Miaoping		Basalt (P_2^1)
9	SL-01	Granite	At the Niubeishan, Xinchang		Indosinian period (γ_5^1)
10	SL-26	Potassium feldspar granite	At Sanxing, Fengle, Shimian		The late Proterozoic (P_t^3, γ_{k2}^3)
11	SL-22	Granite	Beside Dadu River, ShimianTownship's west		The late Proterozoic (P_t^3, γ_2^3)
12	SD-09	Quartz	A quartz vein in ore body I-8		Yanshanian (J_2-K_2)
13	SD-65-1	Dolomite	A dolomite vein in ore body I-8		
14	SD-55-py	Pyrite (py)	Ore body I-10		
15	SD-55-Pr	Pyrrhotite (pr)	Ore body I-10		
16	SD-57	Altered host rock	Ore body I-10 's hanging wall		
17	sD-59	Ore	Ore body I-10		

Series #	($\times 10^{-6}$)															
	La	Ce	Pr	Nd	Sm	Eu	Gd	Tb	Dy	Ho	Er	Tm	Yb	Lu	Y	Sc
1	31.81	55.57	6.41	25.15	4.53	1.04	4.87	0.67	2.90	0.59	1.49	0.18	1.20	0.19	13.27	10.82
2	11.88	25.40	3.45	15.70	3.79	1.64	4.67	0.67	4.14	0.83	1.79	0.22	1.32	0.17	16.39	48.31
3	0.17	0.46	0.04	0.11	0.02	0.02	0.03	0.01	0.03	0.00	0.01	< 0.002	0.01	< 0.002	0.05	3.12
4	5.37	5.68	1.47	4.47	1.24	0.65	l.970	0.30	1.76	0.35	1.10	0.12	0.77	0.12	10.70	0.91
5	0.91	1.57	0.22	0.78	0.16	0.05	0.19	0.03	0.20	0.04	0.65	0.01	0.06	0.01	0.86	0.38
6	0.66	1.01	0.16	0.58	0.13	0.04	0.15	0.02	0.15	0.02	0.05	0.01	0.05	0.01	0.59	0.38
7	25.24	44.44	5.28	19.52	3.81	0.90	4.09	0.70	3.10	0.63	1.75	0.25	1.45	0.20	16.61	8.86
8	30.43	51.45	6.56	24.70	4.70	1.16	4.89	0.68	2.92	0.58	1.51	0.20	1.22	0.17	14.61	12.46
9	19.33	35.88	4.18	15.20	2.90	1.04	2.64	0.40	2.48	0.53	1.50	0.23	1.49	0.22	13.54	18.91
10	79.61	151.00	16.50	65.20	12.82	0.22	15.20	2.53	12.51	2.65	7.03	0.99	6.42	1.05	61.89	3.22
11	85.66	156.10	16.85	66.47	10.96	1.13	11.53	1.68	6.96	1.40	3.71	0.51	3.15	0.51	32.56	9.12
12	0.39	1.23	0.12	0.38	0.08	0.06	0.10	0.02	0.01	0.02	0.03	0.01	0.04	0.01	0.26	0.91
13	10.97	28.35	4.55	23.04	6.59	1.09	7.39	l.200	7.06	1.52	3.81	0.44	2.64	0.41	34.43	3.12
14	0.32	0.77	0.10	0.37	0.10	0.04	0.11	0.03	0.18	0.03	0.06	0.01	0.07	0.01	0.46	2.41
15	0.34	0.79	0.10	0.38	0.10	0.02	0.11	0.02	0.12	0.02	0.04	0.01	0.06	0. 08	0.31	1.69
16	1.59	4.70	0.73	2.39	0.73	0.44	0.75	0.14	0.68	0.13	0.27	0.04	0.36	0.06	1.94	49.05
17	0.23	0.77	0.09	0.36	0.13	0.08	0.13	0.02	0.12	0.02	0.03	0.00	0.03	0.00	0.21	3.78

Laboratory: China National Geological Test Center; Test method: Plasma Spectroscopy

Table 4 Scandium abundance in different rock types (Li 1976; Liu et al. 1984; Yin 1996a). Note: ()* Number of samples in parentheses

Rock type		Sc ($\times 10^{-6}$)	Data source
Igneous rocks	Ultrabasic	5, 15, 30	
	Basic	20, 24, 40	
	Medium	2.5, 4.0	
	Acid	2, 3, 7 (poor calcium), 14 (rich calcium)	
	Alkaline	3	
Sedimentary rocks	Limestone	0.40 ~ 1.50	
	Sandstone (22-sample average)	< 0.00n%	
	Sandstone	1	
	Pacific manganese nodules (5)*	7 ~ 15	
	American bauxite ore	4 ~ 10	
	Clay (2,886-sample average)	12	
	Argillaceous rock (32-sample average)	10	Li 1976
Metamorphic rocks	Marble	0.47 ~ 0.97	Liu et al. 1984
	Quartzite	1.00 ~ 3.20	Yin 1996a, b
	Metamorphosed shale (10)*	20	
	Schist	1 ~ 3, 10 ~ 20	
	Green schist	20 ~ 30	
	Gneiss	12	
	Amphibole	10 ~ 50	
	Amphibole schist	15	
	Serpentine	10	
	Amphibole (16)*	57	
The Crust		10	
	Continental crust	22	
		30	
Meteorite	Chondrite	5.0 ~ 9.4	
	Achondrite	17 ~ 78	
	Basalt of Lunar Maria	39 ~ 75	

Jiangguanshan alkaline syenite may be the differentiated product of mantle-derived magma. The Jiangguanshan quartz diorite is adjacent to the eastward Jiangguanshan alkaline syenite, and the two are in a gradual transition relationship. The Xinchang granite stock is exposed in a triangle area to the east of the deposit, with an area of 10 km^2.

The chemical composition of Xinchang granite is shown in Table 2. Compared with Xiaoshui ordinary granite and potassium feldspar granite, Xinchang granite is obviously low in silicon, high in aluminum, and rich in calcium and magnesium. In terms of REE composition (Tables 3, 5 & 9, and Fig. 2), the ΣREE of Xinchang granite is extremely low, and Eu shows an insignificant negative anomaly.

The Xinchang granite has a high Sc content of 18.91, which is much higher than the average value of medium-acid rocks in Table 4. The Eu/Sm of Xinchang granite is 0.359, which is close to both the trachybasalt of the Siberian platform in Table 6, and to the Middle and Lower Triassic metabasalts in the area. The Xinchang granite's REE parity ratio, namely its EREE/OREE value, is 2.395, which is much lower than the average value for granite. The REE distribution curve of Xinchang granite is close to that of Permian granite in this region (Fig. 2). The $\delta^{18}O_{SMOW}$‰ of quartz from Xinchang granite is 8.5, which is different from that of S-type granite ($\delta^{18}O_{SMOW}$‰ ≥ 10.0) and just falls within the range of I-type granite (Fig. 4). Its $\delta^{30}Si_{NBS-28}$‰ is − 0.30, which is different from the aforementioned Xiaoshui granite, but within the range of the $\delta^{30}Si_{NBS-28}$‰ values of granite-like rocks (Table 8 & Fig. 3). Xinchang granite has its particularities. The above petrochemical and geochemical characteristics show that the formation of this stock is either closely related to basalt, or evolved from basalt magma, or formed by the remelting and metasomatism of the Late Archean-Early Proterozoic,

Table 5 REE eigenvalues of different rocks in the study area

Series #	Sample ID	ΣREE($\times 10^{-6}$)	ΣREE + Y ($\times 10^{-6}$)	ΣLREE/ΣHREE	EREE/OREE	Sm/Nd	Eu/Sm	$(La/Yb)_N$	$(Ce/Yb)_N$	Eu*	δEu
1	SL-05	136.60	149.87	10.30	2.34	0.18	0.23	15.74	9.36	19.18	0.74
2	SD-56	75.67	92.06	4.48	3.01	0.24	0.43	5.34	3.89	17.01	1.32
3	SL-11	0.91	0.96	9.55	2.76	0.21	0.63	17.00	15.16	0.11	1.88
4	SL-18	25.37	36.07	2.91	2.03	0.28	0.52	4.14	1.49	6.28	1.42
5	SD-49	4.28	5.15	6.16	2.39	0.21	0.313	9.31	5.48	0.71	0.97
6	SD-69	3.05	3.64	5.48	2.31	0.22	0.30	7.72	4.03	0.56	0.92
7	SL-03	111.36	127.97	8.15	2.35	0.20	0.24	10.34	6.20	16.12	0.77
8	SL-10	131.13	145.74	9.81	2.30	0.19	0.25	14.81	8.52	19.64	0.81
9	SL-o1	88.02	101.56	8.28	2.40	0.19	0.36	7.70	4.87	11.51	1.24
10	SL-26	373.73	438.62	6.73	2.61	0.20	0.02	7.36	4.75	56.57	0.05
11	SL-22	366.62	399.18	11.45	2.40	0.17	0.10	16.15	10.02	46.00	0.34
12	SD-09	2.48	2.74	9.75	3.04	0.21	0.72	5.90	6.37	0.36	2.18
13	SD-65-1	99.06	133.49	3.05	3.91	0.29	0.17	2.47	2.17	28.40	0.53
14	SD-55-Py	2.19	2.65	3.48	3.14	0.27	0.36	2.94	2.41	0.43	1.15
15	SD-55-Pr	23,116.00	2.46	4.57	3.09	0. 261	0.20	3.64	2.86	0.42	0.65
16	SD-57	13.02	14.97	4.35	3.15	0.31	0.60	2.62	2.64	3.05	1.98
17	SD-59	2.02	2.23	4.68	3.51	0.37	0.60	4.24	4.88	0.54	2.04

Series #	Ce*	δCe	$(La/Lu)_N$	$(La/Sm)_N$	$(Gd/Lu)_N$	Sm/Eu	La/Yb	La/Sm	Sm*	δSm	$(Gd/Yb)_N$
1	76.412	0.77	16.22	4.39	2.56	4.36	26.51	7.02	28.08	0.81	2.49
2	32.938	0.82	6.77	1.96	2.75	2.31	9.00	3.14	24.32	0.78	2.17
3	0.435	1.12	8.43	4.53	1.50	1.60	29.00	7.25	0.20	0.61	3.03
4	14.516	0.42	4.34	2.71	1.64	1.91	6.97	4.33	8.18	0.76	1.57
5	2.323	0.72	8.80	3.55	1.90	3.20	15.66	5.68	0.99	0.81	2.01
6	1.701	0.63	9.16	3.28	2.20	3.32	12.98	5.25	0.75	0.85	1.85
7	61.438	0.77	12.23	4.14	2.05	4.23	17.41	6.63	22.53	0.85	1.73
8	74.881	0.73	17.34	4.05	2.88	4.05	24.94	6.47	28.53	0.82	2.46
9	47.620	0.80	8.51	4.17	1.20	2.79	12.97	6.67	19.79	0.73	1.09
10	193.141	0.83	7.35	3.88	1.45	58.27	12.40	6.21	55.84	1.15	1.45
11	204.053	0.81	16.27	4.89	2.26	9.70	27.19	7.82	63.13	0.87	2.24
12	1.105	1.18	4.69	2.99	1.25	1.40	9.92	4.78	0.71	0.57	1.58
13	36.099	0.84	2.59	1.04	1.80	6.05	4.16	1.67	26.67	1.24	1.72
14	0.912	0.90	2.84	2.03	1.03	2.75	4.95	3.25	0.56	0.89	1.07
15	0.950	0.89	4.17	2.17	1.33	4.95	6.14	3.48	0.45	1.09	1.16
16	5.528	0.90	2.40	1.35	1.18	1.67	4.41	2.16	3.03	1.21	1.28
17	0.740	1.11	3.68	1.07	2.12	1.66	7.13	1.71	0.85	0.78	2.44

① ΣHREE does not contain Y; ② EREE/OREE is parity ratio, namely, (Ce + Nd + Sm + Gd + Dy + Er + Yb)/(La + Pr + Eu + Tb + Ho + Tm); ③Sample theoretical value $Eu^* = (Sm + Gd)_N/2$, $\delta Eu = (Eu)_N/Eu^*$, $Ce^* = (La + Pr)_N/2$, $\delta Ce = (Ce)_N/Ce^*$, $Sm^* = (Nd + Eu)_N/2$, $\delta Sm = (Sm)_N/Sm^*$

Permian, or Middle-Lower Triassic metabasalt in the region.

There are a large number of quartz, carbonate, and diabase veins, as well as a small amount of granitoid aplite, granite pegmatite, and lamprophyre dikes, etc. in the study area's various metamorphic and intrusive rocks of different ages. No Yanshanian intrusive bodies were exposed in the study area.

Different types of mineral resources in the region are very rich; many of these are well known, including Ti, V, Cu, Pb, Zn, SM (scattered metals), REE, coal, asbestos, and the Panzhihua vanadium titano-magnetite deposit (Luo et al. 1996; Yin 1996a).

Table 6 Eu/Sm ratios of different rock types around the world (Li 1976; Liu et al. 1984; Yin 1996a)

Rock type	Oceanic	Siberian platform		Bulgaria	The crust	Granite	Europe & Japan Paleozoic shale	Sedimentary rock
	Olive basalt	Basalt	Trachybasalt					
Eu/Sm	0.44	0.32	0.36	0.28	0.16	0.16	0.17	0.20

Table 7 EREE/OREE ratios of different rocks around the world

Rock type	Chondrite	Chondrite	Chondrite	Ultrabasic rock	Gabbro	Basalt	Diorite	Andesite	Granite
EREE/OREE	3.91	3.88	3.79	3.44	3.22	2.83	2.46	2.14	2.71

Rock type	The crust	Sedimentary rocks		Paleozoic shale	Shale	
		Australia	Northern Guangxi, China	Europe	Russian platform	North America
EREE/OREE	2.70	2.61	2.52	2.61	2.59	2.80

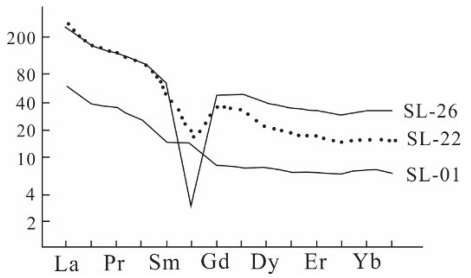

Fig. 2 The chondrite-normalized REE diagram of granites in different geological ages in the region

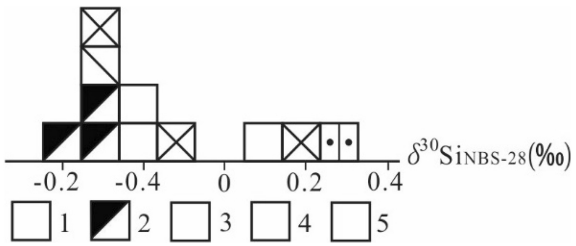

Fig. 3 Silicon isotope histograms of different rocks and minerals in the study area. 1-schist/slate; 2-quartz; 3-biotite; 4-muscovite; 5-granite

Table 8 Silicon isotopic content of different rocks and minerals in the study area. (Note: Chemical compositions of the samples series # are shown in Table 2)

Series #	Sample ID	Sample type	Sample location	$\delta^{30}Si_{NBS-28}$‰	Note
1	SL-19	Schist	Near Tizigou outside the deposit (T_{1-2})	− 0.2	
2	SD-38	Plate	In the footwall of #I-1 ore body (T1-2)	0.1	Protolith: Basalt
3	SD-60	Plate	In the footwall of #I-10 ore body (T1-2)	− 0.2	
4	SL-11	Quartz	From a toumaline-quartz vein at Liushapo	− 0.4	
5	SD-26	Quartz	Orebody I-4	− 0.3	
6	SD-67	Quartz	Orebody I-7	− 0.3	
7	SD-20	Biotite	Pyrrhotite vein III-3	− 0.3	
8	SD-23	Muscovite	Orebody I-4	0.3	
9	SL-01	Granite (γ_5^1)	Niubeishan, Xinchang	− 0.3	I type
10	SL-22	Granite (Pt_3)	Beside the Dadu river	− 0.1	S type
11	SL-26	Granite (Pt_3)	Sanxing village, Fengle township	0.2	

Table 9 Chondrite-normalized REE values of different minerals and rocks from the study area

Series #	Sample ID	La	Ce	Pr	Nd	Sm	Eu	Gd	Tb	Dy	Ho	Er	Tm	Yb	Lu
1	SL-05	99.41	59.12	53.42	41.92	22.65	14.25	15.71	13.40	9.36	8.08	7.10	5.46	6.32	6.13
2	SD-56	37.13	27.02	28.75	26.17	18.95	22.47	15.07	13.40	13.36	11.37	8.52	6.67	6.95	5.48
3	SL-11	0.54	0.49	0.33	0.19	0.12	0.21	0.10	0.10	0.10	0.06	0.03	0.06	0.03	0.07
4	SL-18	16.78	6.04	12.25	7.45	6.20	8.90	6.36	6.00	5.68	4.80	5.24	3.64	4.05	3.87
5	SD-49	2.84	1.67	1.81	1.30	0.80	0.69	0.61	0.66	0.63	0.48	0.31	0.33	0.31	0.32
6	SD-69	2.07	1.08	1.33	0.97	0.63	0.52	0.50	0.48	0.48	0.33	0.26	0.21	0.27	0.23
7	SL-03	78.88	47.28	44.00	32.53	19.05	12.33	13.19	14.00	10.00	8.63	8.33	7.58	7.63	6.45
8	SL-10	95.09	54.73	54.67	41.17	23.50	15.89	15.77	12.80	9.42	7.95	7.19	6.06	6.42	5.48
9	SL-01	60.41	38.17	34.83	25.33	14.50	14.25	8.52	8.00	8.00	7.26	7.14	6.97	7.84	7.10
10	SL-26	248.78	160.64	137.50	108.67	64.10	3.01	49.03	50.60	40.36	36.30	33.48	30.00	33.79	33.87
11	SL-22	267.69	166.06	140.42	110.78	54.80	15.48	37.19	33.60	22.45	19.18	17.67	15.46	16.58	16.45
12	SD-09	1.21	1.31	1.00	0.63	0.41	0.80	0.32	0.36	0.03	0.23	0.16	0.18	0.21	0.26
13	SD-65-1	34.28	30.16	37.92	38.40	32.95	14.93	23.84	24.00	22.77	20.82	18.14	13.33	13.90	13.23
14	SD-55-Py	1.01	0.82	0.82	0.62	0.50	0.49	0.37	0.50	0.58	0.38	0.28	0.27	0.34	0.36
15	SD-55-Pr	1.08	0.85	0.83	0.63	0.50	0.27	0.34	0.38	0.39	0.27	0.21	0.24	0.30	0.26
16	SD-57	4.96	5.00	6.10	3.99	3.67	6.03	2.43	2.76	2.19	1.81	1.27	1.33	1.90	2.07
17	SD-59	0.71	0.82	0.77	0.61	0.67	1.10	0.41	0.44	0.39	0.21	0.13	0.18	0.17	0.19
Chondrites		0.32	0.94	0.12	0.60	0.20	0.07	0.31	0.05	0.31	0.07	0.21	0.03	0.19	0.03

2.4 Structure

Remote sensing interpretation shows that linear and annular structures develop in the study area. Linear structures can be divided into the following groups: NW, NNE, NS, NWW, and NEE. These linear structures include the following two important ductile shear zones, the Daduhe ductile shear zone, and the Xiyoufang ductile shear zone[1].

The identification of annular structures is helpful for the discovery of deep hidden magmatic activities or structural thermal anomalies, which in turn help to determine the metallogenic mechanism. As the largest known annular structure in the area, the Xiyoufang annular structure is concentric with the Xiyoufang as the center, at a diameter of about 8 km. Its southern point can reach the Dashuigou deposit. The Xiyoufang annular structure is a composite ring. In addition to the concentric composite ring of the large ring itself, there are two small annular structures with a diameter of about 2 km inside the large ring. It is also accompanied by two other small rings around it.

The annular structure is strongly intersected by linear structures with different directions and different mechanical properties, forming the Ø-shaped structures that are very favorable for mineralization. The Xiyoufang annular structure is closely related to mineralization. Nearly 20 tellurium mineralization showings and the Dashuigou tellurium deposit, as well as more than 10 Au-Bi composite geochemical anomalies and some gold geochemical anomalies, are spatially related to the annular structure.

Located within the southwest of the Xiyoufang annular structure and as one of the sub-rings of the Xiyoufang annular structure, the Dashuigou annular structure intersects with NE, EW, SN, and NW trending linear structures, forming a characteristic Ø-shaped structure and controlling the Dashuigou tellurium deposit and the nearby Majiagou tellurium showing, as well as several Au and Bi geochemical anomalies.

The perfectly circular Jinhuadong annular structure is also a sub-ring of the Xiyoufang annular structure. It intersects with NWW, NNW, and SN-trending linear structures, forming a characteristic Ø-shaped structure, and

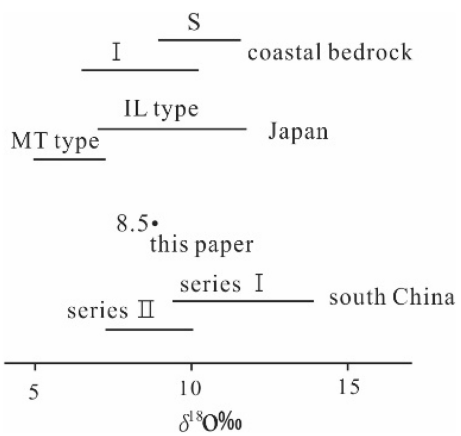

Fig. 4 The $\delta^{18}O‰$ diagram of different types of granites from different regions

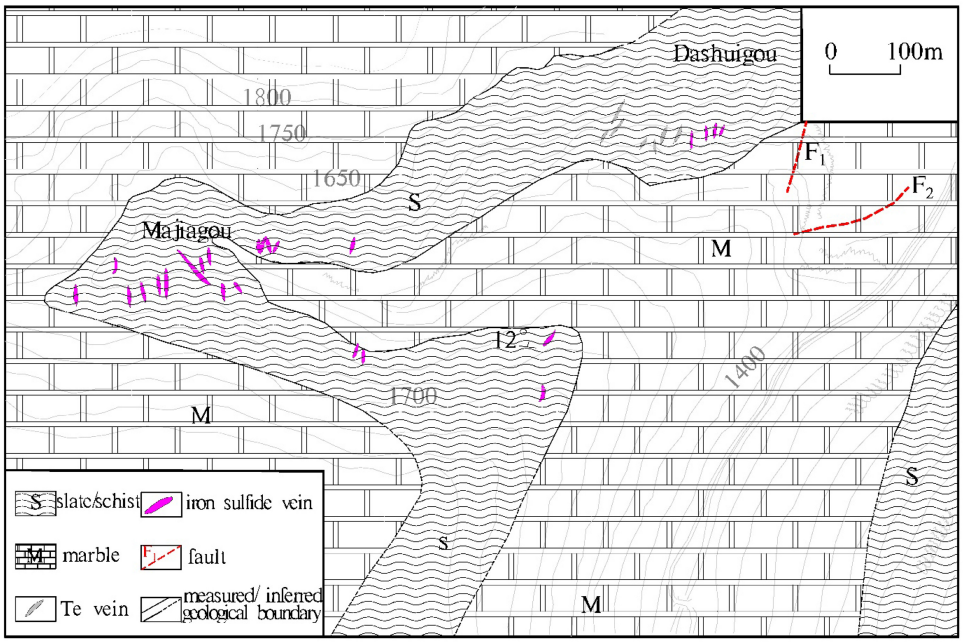

Fig. 5 Deposit geology (Yin 1996a)

controls the Jinhuadong, Qifenyao, and Bafenyao tellurium showings, as well as several Au and Bi geochemical anomalies.

In addition, there are Baita, Tianwan Township, Tangjiapo, and Jiangguanshan ring structures. The common feature of these annular structures is their close spatial relationship with the Bi and Au geochemical anomalies.

The folds in the study area are mostly NNE or nearly SN-trending, and are relatively tight, narrow, and long. These folds include the Dashuigou dome structure and the Bindo anticline in the northwest of the deposit, etc. The Dashuigou dome is roughly NNE trending, more than 10 km long, and entirely composed of Middle and Lower Triassic metamorphic rocks. Its northern section is damaged by a fault of nearly the same strike, and its four sides of the northeast, southwest, northwest, and NNW are cut and bounded by NNW-trending, near-north–south, and NNE-trending faults respectively, forming a highly flattened rhombic block in space. On the two-dimensional plane, the Dashuigou tellurium deposit is located in the north-central part of the dome.

The representative faults in the study area include the Hongba fault, Wanbahe fault, Xiyoufang-Guanyinshan fault, Keluo-Jiziping fault, and Anshunchang-Xinchang fault from west to east. On the whole, these faults are broom-shaped converge at the northern end and spread out at the southern end.

3 Deposit geology

The deposit's host rocks include marble, slate, and schist of the lower-middle Triassic system, which is a set of littoral-epicontinental faces of carbonate-basic volcanic rocks but has suffered regional low-temperature dynamic metamorphism during the Indosinian orogeny, forming a low-greenschist facies metamorphic rock system (Fig. 5, Yin 1996a).

The Triassic stratigraphic sequence of the Dashuigou tellurium deposit is as follows:

i. Schist and slate formation at the top
ii. Large-thick fine-grained marble in the upper part
iii. Schist and slate formation in the middle
iv. Medium-fine-grained striated/banded marble in the lower part
v. Coarse to large-grained thick marble at the bottom

Schist and slate formation in the middle is the deposit's main direct host rock, including hornblende schist, garnet schist, tourmaline schist, and chlorite schist, in which exists a well-developed 10–15 m wide fault zone. An approximately 3 m wide tourmaline-quartz vein develops in the fault zone. All of the Triassic strata make up the NNE-trending Dashuigou dome as mentioned above. Both the geological and geochemical characteristics in the area indicate that protolith of the tellurium ore veins' direct host rocks is poorly differentiated, mantle-derived basalt.

The deposit is located at the northeastern end of the Triassic metamorphic dome. The tellurium ore veins are both controlled by and fill a group of shear fractures, which

strike from 350 to 10 degrees and dip at 55 to 70 degrees westward. Widths of the ore bodies, which are in the shape of lenticular veins and have sharp contact with their host rocks, vary between 25 and 30 cm.

Both faults and folds are well-developed in the area. The annular and linear structures together make up special Ø-shaped structures which control the formation of different types of endogenetic mineral deposits in the area, including the Dashuigou tellurium deposit. No intrusive rocks occur within a 5 km radius around the deposit. Only two small Permian ultrabasic-basic rock bodies emerge within a 10 km range of the deposit as described above.

The altered host rocks occur in narrow bands ranging between several centimeters and one meter in thickness. Altered zones beside the massive ore veins are narrower at only several centimeters wide. The dominant alterations include dolomitization, silicification, biotitization, muscovitizaion, tourmalinization, sericitizaion, greisenization, and chloritization (Chen et al. 1994a, b; Yin et al. 1994a, b, c; 1996a, b; Yin 1996a, b). More than thirty minerals are identified in the ore, which includes tetradymite, pyrrhotite, pyrite, dolomite, quartz, chalcopyrite, tsumoite, tellurobismuthite, galena, magnetite, gold, silver, electrum, ilmenite, calcite, calaverite, siderite, magnesite, rutile, muscovite, biotite, sericite, hornblende, chlorite, plagioclase, K-feldspar, tourmaline, hematite, garnet, apatite, and epidote, of which the first five minerals are the most important and comprise 85% of the ore (Yin et al. 1994a, b, c; Yin 1996a; Yin and Shi 2019). The Te content in the ore varies between 0.01 and 34.58% (Yin 1996a). Replacement, remnant, reaction border, and granular are the dominating textures of the ore. Massive, vein/veinlet, and stockwork veins are the dominating structures of the deposit. Two mineralization stages and five sub-stages exist in the deposit (Yin 1996a; Yin and Shi 2019, 2020): The Pyritic stage includes three mineralization sub-stages: carbonate sub-stage (I) → pyrrhotite sub-stage (II) → chalcopyrite sub-stage (III) (from early to late); the Tellurium stage includes two mineralization sub-stages: tetradymite sub-stage (I) → tsumoite (BiTe0.97) sub-stage (II) (Yin 1996a).

4 Sampling and analytical methods

4.1 Field sampling

Fresh samples were collected from the proper locations of the deposit's typical host and country rocks. They were described in detail on site, then properly labeled or numbered and wrapped with waxed paper to avoid cross-contamination with other samples in the same sample box, and finally packed and shipped to the work laboratory.

4.2 Lab sample preparation

In the lab, all rock samples were sorted, air-dried, and 2-stage crushed to minus 10 mesh, then a split 250 g (approximate) sub-sample was pulverized on a ring mill pulverizer to 95% − 140 mesh. The sub-sample was weighed, rolled, homogenized, and bagged in a pre-numbered bag.

4.3 Analytical methods

4.3.1 Multi element ICP Analysis/LA-ICP-MS

A 0.5-g sample was digested with 3 ml of a 3:1:2 ($HCl:HNO_3:H_2O$) containing beryllium for 90 min in a water bath at 95 °C. The sample was then diluted to 10 ml with water. The sample was analyzed on a Jarrell Ash ICP unit. The entire set of samples was redone if the quality control standard fell outside 2 standard deviations or if the blank was greater than the limit. Results were collated by computer and printed alongside accompanying quality control data (repeats and standards).

4.3.2 Silicon isotope analysis

Excitation probe method, 30 ∼ 100 μg Si (± 0.1‰), $SiO_2 + 2BrF_5$ & $O_2 + 2BrF_3 + SiF_4$; reference material: NBS-28, $\delta^{30}Si_{NBS-28}‰ = 0$; rose quartz, $\delta^{30}Si_{NBS-28}‰ = -0.28$; IRMM-018, $\delta^{30}Si_{NBS\text{-}28}‰ = 0.0$.

4.3.3 Oxygen isotope analysis

Continuous flow Gasbench II-IRMS online analytical method, ± 0.2‰, thermostat sample pan temperature 28 °C, Chromatography column temperature 45 °C, He pressure 12f0 kPa.

4.3.4 Strontium isotope analysis

MC-ICP-MS instrument for the isotope analysis, Standard-Sample-Bracketing method was used to correct the instrumental mass bias.

5 Chemistry of the host rocks

5.1 Petrochemical characteristics

Chemical compositions of the deposit's host rocks are listed in Table 10 and discussed as follows.

Similar to the mantle origin of the intrusive rocks in the study area as mentioned above, the direct ore-hosting wall rocks of the deposit also originate from the upper mantle. As seen in Table 10, the host rocks have the following

Table 10 Petrochemical compositions of the deposit's host rocks (%)

Series #	1	2	3	4	5	6	7	Average
Sample id	SL-12	SL-19	SD-01	SD-38	SD-43	SD-56	SD-60	
Sample type	Schist	Schist	Slate	Slate	Schist	Slate	Slate	
Sample location	Miaoping	Near Miaoping	Orebelt II's EB	OredobyI-1's FW	OredobyI-1's HW	OredobyI-10's HW	OredobyI-10's FW	
SiO_2	41.48	52.12	48.74	42.80	43.16	45.38	32.30	43.71
Al_2O_3	12.54	13.67	12.93	12.71	15.45	14.98	16.75	14.15
TiO_2	1.54	0.65	2.43	1.64	2.71	1.83	1.93	1.82
Fe_2O_3	1.75	1.16	5.15	3.05	3.06	4.04	4.07	3.18
FeO	10.27	4.10	10.99	9.10	12.26	9.51	12.43	9.81
CaO	8.30	6.84	9.86	13.06	8.74	11.35	11.38	9.93
MgO	5.76	3.22	5.52	6.85	6.97	6.93	7.77	6.15
K_2O	1.61	3.32	0.20	0.12	0.14	0.20	3.84	1.35
Na_2O	0.79	1.10	1.59	1.18	1.51	2.01	0.44	1.23
MnO	0.28	0.09	0.21	0.22	0.21	0.18	0.25	0.21
P_2O_5	0.10	0.08	0.20	0.10	0.25	0.12	0.15	0.14
CO_2	12.47	9.15	0.20	6.62	2.08	1.06	5.42	5.29
H_2O^+	2.94	1.16	0.77	1.38	2.53	0.58	1.12	1.50
H_2O^-	0.14	0.25	0.12	0.12	0.17	0.08	0.28	0.17
Organic carbon	0.33	4.53	0.38	0.98	0.81	1.13	0.55	1.24
Total	100.30	101.44	99.29	99.93	100.05	99.38	98.68	99.88

EB-east boundary, FW-foot wall, HW-hanging wall

Table 11 Chemical compositions of the metamorphosed basalt in the deposit's western periphery (wt.%)

Sample ID/type	SiO_2	Al_2O_3	TiO_2	Fe_2O_3	FeO	CaO	MgO	Data source
SL-10	33.16	5.19	0.53	0.41	2.25	25.45	4.19	This paper
Olive basalt (5)*	46.77	11.64	2.52	5.99	6.65	9.17	9.55	Shen et al. 1985
Sample ID/type	K_2O	Na_2O	MnO	P_2O_5	CO_2	H_2O^+	H_2O^-	Data source
SL-10	1.2	0.58	0.11	0.04	26.41	0.83	0.08	This paper
Olive basalt (5)*	0.96	2.56	0.2	0.264				Shen et al. 1985

*Average value of 5 olive basalt samples from the Panzhihua-Xichang rift

petrochemical characteristics: low SiO_2 content varying between 32.30% and 52.12% with an average of 43.71%, Al_2O_3 varying between 12.54% and 16.75% with an average of 14.15%, low Na_2O(< 4.00%)and K_2O where the average content of K_2O is generally similar to that of Na_2O. Total iron FeO*/(FeO* + MgO) = 0.68, $CaO/Al_2O_3 = 0.70 < 0.82$, $Fe^{3+}/Fe^{3+} + Fe^{2+} = 0.23 < 0.40$, with features of the mantle-derived volcanic rocks. Compared to the basalt in the Panzhihua-Xichang Rift (Table 11), which is about 200 km away from the deposit, its host rock is relatively poor in TiO_2, Fe_2O_3, MgO, Na_2O, and P_2O_5, but rich in FeO, CaO, and K_2O.

It is generally believed that except for metamorphic rocks accompanied by metasomatism such as various altered rocks and migmatites, chemical compositions of all other metamorphic rocks that result from certain protolith under relatively closed environments remain the same before and after the metamorphism. As a result, both the petrochemical and geochemical characteristics of such metamorphic rocks essentially reflect that of the protolith. As mentioned above, the rocks in the study area are mainly low greenschist facies of metamorphic rocks, were unaffected by any geological event after the metamorphism, and should be in the same chemical system as the protolith. Protolith of these metamorphic rocks should be basic volcanic rocks, namely basalt. This is consistent with the previous conclusions based on its geological characteristics.

Table 12 The calculated molecular numbers of chemical constituents of the deposit's host rocks

Series #	Sample id	SiO_2	Al_2O_3	TiO_2	Fe_2O_3	FeO	CaO	MgO	K_2O	Na_2O	MnO	P_2O_5	CO_2	H_2O^+	H_2O^-
1	SL-12	691	123	19	11	143	148	144	17	13	4	1	283	163	8
2	SL-19	869	134	8	7	57	122	81	35	18	1	1	208	64	14
3	SD-01	812	127	30	32	153	176	138	2	26	3	1	5	18	7
4	SD-38	713	125	21	19	126	233	171	1	19	3	1	150	77	7
5	SD-43	197	151	34	19	170	156	174	1	24	3	2	47	141	9
6	SD-56	756	147	23	25	132	203	173	2	32	3	1	24	32	4
7	SD-60	538	164	24	25	173	203	194	41	7	4	1	123	62	16
Average		654	139	23	20	136	177	154	14	20	3	1	120	80	9

Table 13 The calculated A, C and F values of different rock samples from the deposit's host rocks

Series #	Sample ID	A'	C'	F'	$\sum$	A	C	F	Falling area in Fig. 6	Protolith
1	SL-12	104.0	145.0	291.0	540.0	19.3	26.9	53.9	2	Basic rcok
2	SL-19	88.0	119.0	139.0	346.0	25.4	34.4	40.2	2	Basic rcok
3	SD-01	131.0	173.0	294.0	598.0	21.9	28.9	49.2	2	Basic rcok
4	SD-38	124.0	230.0	300.0	654.0	19.0	35.2	45.9	2	Basic rcok
5	SD-43	145.0	149.0	347.0	641.0	22.6	23.2	54.1	2	Basic rcok
6	SD-56	138.0	200.0	308.0	646.0	21.4	31.0	47.7	2	Basic rcok
7	SD-60	141.0	200.0	371.0	712.0	19.8	28.1	52.1	2	Basic rcok
Average		124.0	174.0	293.0	591.0	21.3	29.7	49.0	2	Basic rcok

A' = $(Al_2O_3 + Fe_2O_3)$-$(Na_2O + K_2O)$, C' = CaO-3.3*P_2O_5, F' = MgO + MnO + FeO; Σ = A' + C' + F', C = C'/Σ, F = F'/Σ, A = A'/Σ, A + C + F = 100

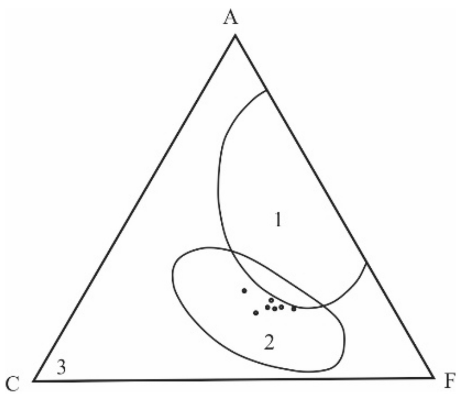

Fig. 6 The ACF plot of the deposit's host rocks (Miyashiro 1973). 1. Shale and greywacke; 2. Basalt and andesite; 3. limestone

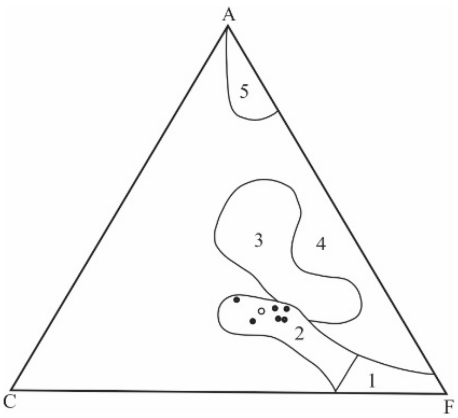

Fig. 7 The ACF diagram of the deposit's host rocks (Winkler 1979). 1. Ultrabasic rock area; 2. Basic rock area; 3. greywacke area; 4. clay and shale area without or with 35% carbonate; 5. aluminous clay and shale area

The following petrochemical parameters of the direct ore-hosting rocks of the deposit also prove that they originated from the upper mantle.

The A, C, and F values based on the molecule numbers in Table 13 are calculated by converting the weight percentages of various chemical components of different samples in Table 10 into molecule numbers (= weight percent divided by their respective molecular weights), then multiplying by 1,000 to eliminate decimals (Table 12).

The A, C, and F values in Table 13 are projected on the ACF diagrams in Figs. 6 and 7. The Middle and Lower

Table 14 The calculated Niggli's values of different rock samples from the deposit's host rocks

Series #	Sample ID	al'	fm'	c'	alk'	Σ	al	fm	c	alk	mg	k	c'/fm	si	h	CO_2	O	Ti
1	SL-12	123.00	313.00	148.00	30.00	614.00	20.00	51.00	24.00	5.00	0.46	0.57	0.47	112.54	27.85	46.09	0.07	3.09
2	SL-19	134.00	153.00	122.00	53.00	462.00	29.00	33.00	26.00	12.00	0.53	0.66	0.80	188.10	16.88	45.02	0.09	1.73
3	SD-01	127.00	358.00	176.00	28.00	689.00	18.00	52.00	26.00	4.00	0.39	0.07	0.49	117.85	3.63	0.73	0.18	4.35
4	SD-38	125.00	338.00	233.00	20.00	716.00	17.00	47.00	33.00	3.00	0.51	0.05	0.69	99.58	11.73	20.95	0.11	2.93
5	SD-43	151.00	385.00	156.00	25.00	717.00	2 1	54.00	22.00	3.00	0.45	0.04	0.41	100.28	20.92	6.56	0.10	4.74
6	SD-56	147.00	358.00	203.00	34.00	742.00	20.00	48.00	27.00	5.00	0.48	0.06	0.57	101.28	4.85	3.23	0.14	3.10
7	SD-60	164.00	421.00	203.00	48.00	836.00	20.00	50.00	24.00	6.00	0.46	0.85	0.48	64.35	9.33	14.71	0.12	2.87
Average		139.00	332.00	177.00	34.00	682.00	21.00	48.00	26.00	5.00	0.47	0.33	0.56	112.08	13.60	19.61	0.12	3.26

al' = Al_2O_3 + Cr_2O_3, fm' = FeO + 2*Fe_2O_3 + MgO + MnO + NiO, C' = CaO + BaO + SrO, alk' = Na_2O + K_2O + Li_2O; Σ = al' + fm' + c' + alk', al = (al'/Σ)*100, fm = (fm'/Σ)*100, c = (c'/Σ)*100, alk = (alk'/Σ)*100, al + fm + c + alk = 100; Mg = MgO/fm, k = K_2O/alk, si = 100*SiO_2/Σ, h = 100*(H_2O^+ + H_2O^-)/Σ, CO_2 = 100*CO_2/Σ, O = 2*Fe_2O_3/fm, Ti = 100*TiO_2/Σ

Triassic ore-host metamorphic rocks' protolith in the study area also fall into the basalt area, which was defined respectively by Miyashiro (1973) and Winkler (1979).

The Niggli's values (1954) of chemical compositions from samples in Table 10 were calculated and listed in Table 14, from which Fig. 8 was drawn and on which the two samples with serial numbers 1 and 7 overlap. All samples fell into the positive metamorphic rock area located near both sides of the Bushveld Complex cast line, indicating they result from igneous rocks and not sedimentary rocks. It is thus inferred that the protolith is a partial basic or basic rock with a low degree of differentiation.

According to the SiO_2–(Na_2O + K_2O) diagram (Fig. 9), which was first proposed by Carmichael et al. (1974), 3 samples from the deposit fall into the tholeiite area while the other 4 samples fall into the alkaline basalt area. Among them, the projection point of sample No. 7 falls out of the diagram but still belongs to the alkaline basalt area. The average of all 7 samples also falls in the alkaline basalt area. The alkaline basalt area and the tholeiite are mixed and accumulated and the differentiation is poor, which may indicate that the tectonic movement of the upper mantle and the deep crust during the early and middle Triassic in this area was violent and rapid, and the material activities were complex. This is related to the area's complex tectonic background.

On the (al + fm)-(c + alk) vs. si diagram (Fig. 10), which was first proposed by Simonen (1953), the samples also mainly fall in the volcanic rock area, which further proves that the host rock's protolith is an igneous rock rather than the marine sedimentary rock.

On Jensen's (1976) (FeO + Fe_2O_3 + TiO)–Al_2O_3–MgO diagram (Fig. 11), six of the seven samples fall into the iron-rich tholeiite area, and only one sample falls on the boundary between andesite and dacite.

On the c-mg diagram (Fig. 12) that was first proposed by Leake (1964), these basalts have a typical magmatic evolutionary trend.

In addition, according to the Al_2O_3–(Na_2O + K_2O) diagram of the early Precambrian basic volcanic rocks in China compiled by Zhang (1984), all samples of this study fall into the same area as the Archean-Early Proterozoic metamorphic basic volcanic rocks in China (Fig. 13). This shows that although the two regions are far away from each other and have different rock-mineral assemblages of different geological ages, different tectonic settings, and different degrees of metamorphism, their protolith are all basic volcanic rocks genetically related to mantle-derived magma.

To sum up, the deposit's host rock has the following characteristics: low SiO_2, Na_2O, and K_2O content and $CaO/Al_2O_3 < 0.82$, $Fe^{3+}/(Fe^{3+} + Fe^{2+}) < 0.40$. These

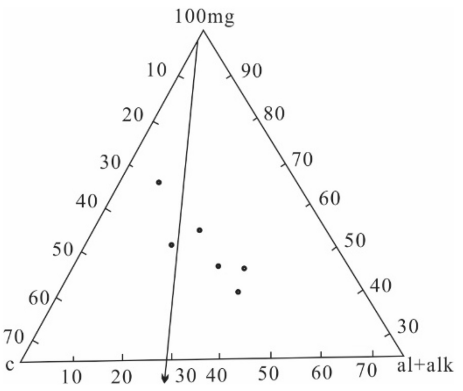

Fig. 8 Tri-linear plot of Niggli's 100 mg-c-(al + alk) of the deposit's host rocks (Carmichael et al. 1974)

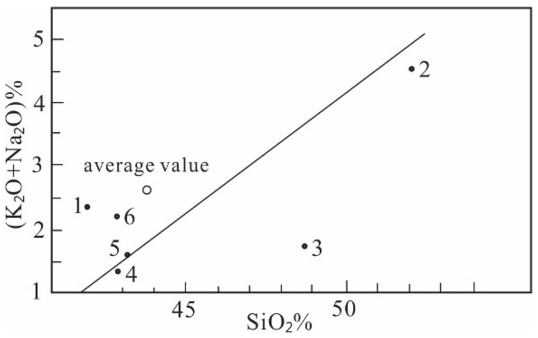

Fig. 9 The SiO_2-(Na_2O + K_2O) plot of the deposit's host rocks (Carmichael et al. 1974). Above the oblique line is the alkaline basalt area, and below the tholeiite area. (The sample numbers in the figure are the same as those in Table 10)

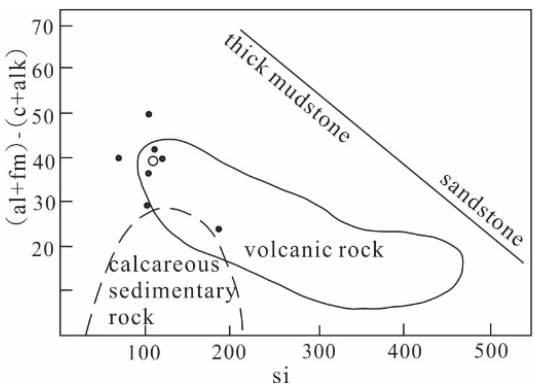

Fig. 10 The [(al + fm)-(c + alk)] vs. si plot of the deposit's host rocks (Simonen 1953). (Note: The open circle in the figure is the average of the 7 samples)

metamorphic rocks are positive metamorphic rocks and their protolith are mantle-derived tholeiite with a low degree of differentiation, which has a typical magmatic evolutionary trend. Its formational environment should be when the crust changes violently and rapidly, and the asthenosphere material in the upper mantle is in a state of non-equilibrium, complex, and rapid exchange, which is roughly equivalent to the subduction of the Indosinian Paleo-Tethys plate to the Yangtze plate.

5.2 Geochemistry of rare earth elements

The rare earth element geochemistry of different host rocks in the mine also proves that they mainly originate from the upper mantle. The rare earth element compositions of different samples collected from the study area are shown in Table 3. According to this table, the chondrite-normalized REE values (Table 9), logarithmic values (Table 15), and various eigenvalues (Table 5) were obtained.

In the following section, the host rock's protolith, formation, and evolution characteristics will be discussed based on the samples' REE abundance and eigenvalues.

Scandium (Sc) is classified as an REE due to both its chemical similarity to and close symbiosis with other REEs in minerals. Sc's outer electron shell is of the same type as REEs. The Sc content in different rock types is not high and is basically fixed within a certain range of values. In addition, it has certain chemical stability, so the rock type can be inferred by Sc's abundance in the rock. For metamorphic rocks, the protolith can be recovered by measuring its Sc abundance, as relevant studies have shown that Sc content in some metamorphic rocks is closely related and proportional. For example, Sc content is the lowest in marble and quartzite, while it is relatively high in metamorphosed basic and argillaceous rocks. There is no carryover of Sc into metamorphic rocks, and the Sc enrichment in some cases is the result of redistribution (Liu et al. 1984).

Table 4 lists the Sc abundance in different rock types, from which it is clear that most of the Sc in the lithosphere exists in basic and ultrabasic rocks. In metamorphic rocks, it mainly exists in amphibolite and greenschist whose protolith is basic-ultrabasic rocks. According to Table 3, the middle-lower Triassic slate in the study area contains (10.82–48.31) $\times$ 10^{-6} Sc, showing a high Sc abundance and indicating that the protolith may be a basic volcanic rock. It is consistent with the conclusion that the protolith is basalt by the above-mentioned petrochemical characteristics.

The tourmaline-quartz vein in the lower part of the host rock contains 3.12 $\times$ 10^{-6} Sc, which is similar to that of the quartzite samples in Table 4. The striped/banded marble in the lower part of the host rock contains (0.38–0.91) $\times$ 10^{-6} Sc, which is also consistent with the Sc content of the marble in Table 4. The coarse-grained

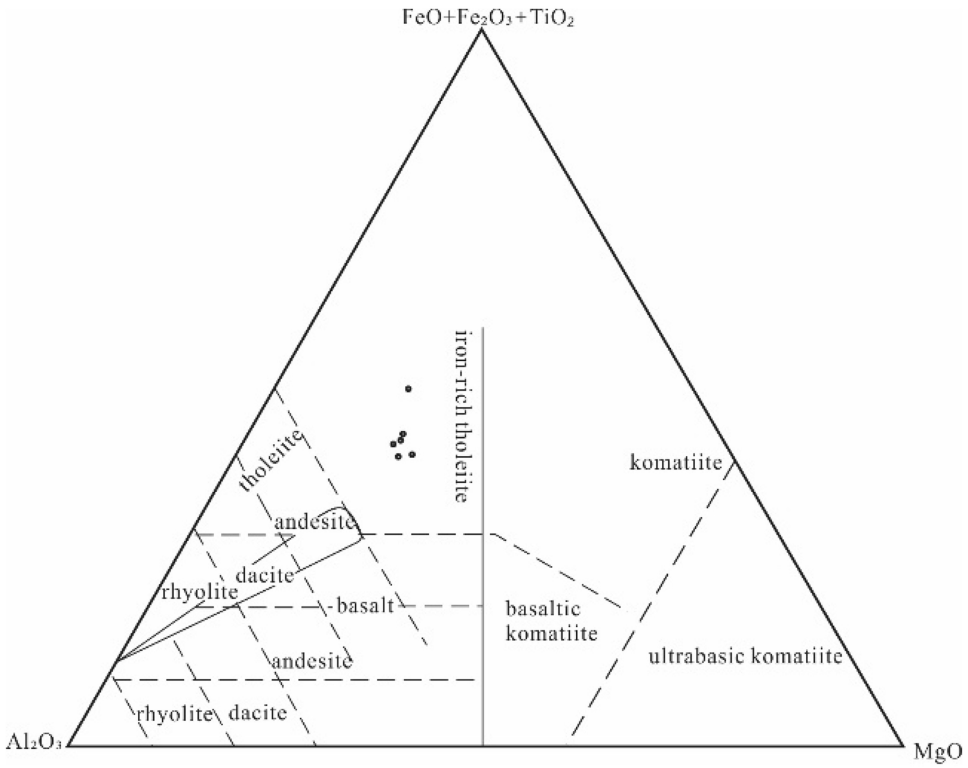

Fig. 11 The $(FeO + Fe_2O_3 + TiO)$-Al_2O_3-MgO triangular plot of the deposit's host rocks (Jensen 1976). (*Note*: weight percentage of the chemical compositions of the rock samples is used, and the composition on the three corners is taken as 100)

marble at the bottom contains 0.38×10^{-6} Sc, which is similar to that of the striped/banded marble.

The Sc content of the two samples from the Upper Permian metabasalt and the upper black rock section in the study area is 12.46×10^{-6} and 8.86×10^{-6} respectively, which are also relatively high. This means that the protolith of the Upper Permian metabasalt and the upper black rock section may also be basic volcanic rocks. This is also indicated by the great similarity between the two in the chondrite-normalized REE model (Fig. 14). The REE eigenvalues of the two are also surprisingly consistent (Table 5), which further proves the above conclusion. The

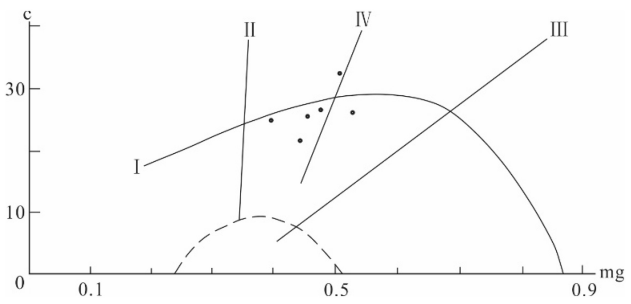

Fig. 12 The c-mg plot of the deposit's host rocks. I- igneous rock evolution trend; II- limestone range; III- dolomite range; IV- evolutionary trend of mixed marl-basalt (amphibolite, calcium silicate and gneiss assemblages) from Granville, Canada (Note: Samples 1 and 7 overlap in the diagram; Leake 1964)

Eu/Sm ratios of the Upper Permian metabasalt and slate (the upper black rock section) are 0.236 and 0.237 respectively (Table 5), with a very small change of only 0.001, which is close to that of trachybasalt in Bulgaria (Table 6).

The parity ratios of these two samples are 2.300 and 2.354 respectively, with an average of 2.357, which is close to that of diorite (Table 7) but slightly lower than that of basalt.

In general, the total REE amount in these two samples is relatively high, the light REEs are enriched, and the heavy REEs are depleted. The curve slopes to the right, the slope is larger, and the δEu is larger (close to 1.0), showing that the Eu anomaly is not obvious (Fig. 14). On the La/Yb-REE plot of rock samples from around the world, both samples fall into the basalt area (Fig. 15).

To sum up, protolith of the Upper Permian metamorphic rocks, especially that of the upper black rock section (P_2^4), are basalt, and both are the products of the same homologous magmatic evolution.

The Eu/Sm ratios of the two Middle-Lower Triassic slate samples in Table 5 are 0.23 and 0.43 respectively, with an average of 0.34, which is very close to that of the Siberian platform basalt (Table 6). This proves that the protolith of this set of rocks is basalt. The parity ratios of these two samples are 2.341 and 3.012 respectively, with an average of 2.677, which is close to that of basalt. It is

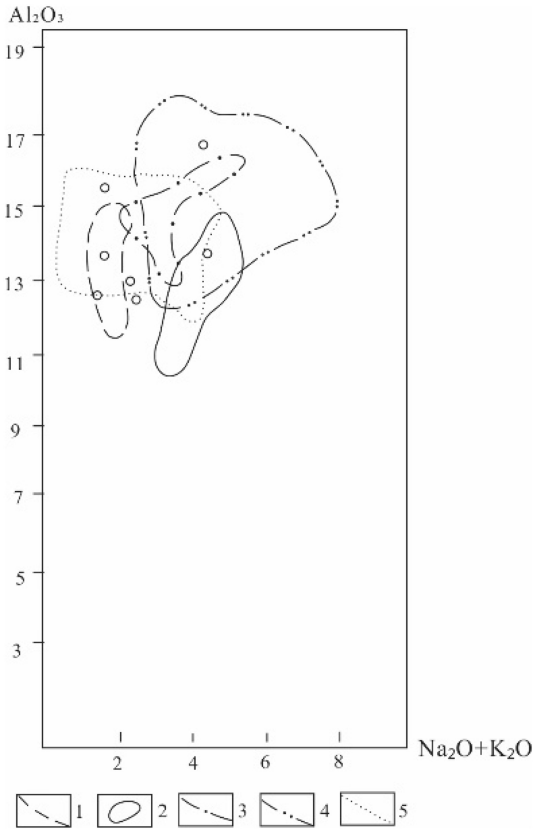

Fig. 13 The Al_2O_3-($Na_2O + K_2O$) plot of the early Precambrian basic volcanic rocks in China (Zhang 1984). 1. Early Proterozoic Wutai region; 2. Early Proterozoic south Liaoning; 3. Archean Anshan of Liaoning; 4. Archean Shandong Peninsular; 5. Archean West Shandong

also similar to that of the North American shale and granite (Table 7), indicating that its origin is more complex. In Fig. 15, both samples fall into the basalt area, indicating that their protolith is basalt. The Sm/Nd ratios of the two slate samples are 0.180 and 0.241 respectively (Table 5). In the graph of Sm/Nd ratios of different rocks (Richard et al. 1976), they are consistent with the Hawaiian alkaline basalt (Fig. 16), indicating that the chemical components of the protolith, namely the basalt, are more complex.

It can also be seen from Fig. 16 that the Sm/Nd ratios (0.19 and 0.195) of the two samples from both the upper Permian metabasalt and the upper black rock section at the deposit's periphery fall into the Hawaiian alkaline basalt area, which is consistent with the results shown in Fig. 15.

The Eu/Sm ratios of the three marble samples from the Middle and Lower Triassic in the study area are 0.524, 0.313, and 302 respectively (Table 5), with an average of 0.380, which is much higher than that of the sedimentary rocks but similar to that of the Siberian platform basalt and trachybasalt (Table 6), with a similar Eu/Sm ratio to its overlying slate. This may mean that these limestones were subjected to considerable thermal action at the time when they received the overlying basalt lava flows. The heat flow not only caused crystallization of these marine limestones to form marbles, but also imprinted these marbles with REEs from basalt magma to a certain extent so that the two have a certain similarity in their REE compositions (Table 5, Fig. 17). The parity ratios of these three samples are 2.03, 2.39, and 2.31 respectively, with an average of 2.23. This is consistent with the parity ratio interval of both the Grenada and Hawaiian basalt and tholeiite in Fig. 16, and also consistent with that of its overlying slate, indicating that they were indeed affected by heat flow from the basalt magma, resulting in REE exchange.

The REE compositions and eigenvalues of the striped/banded marble (sample SD-49) and coarse-grained marble (sample SD-69) within the deposit are very similar (Tables 3 and 5), as are their REE chondrite-normalized models (Fig. 17). On the other hand, the REE composition, eigenvalues (Tables 3 and 5), and REE chondrite-normalized model of the striped marble (sample SL-18, Fig. 17) near Tizigou outside the deposit are quite different from that of samples SD-49 and SD-69 within the deposit. This shows that.

- The lithofacies of the Middle and Lower Triassic rocks in the region vary widely, even across short distances. This indicates that the lithofacies paleogeographic environment at that time was turbulent due to frequent tectonic activities.
- The rocks within the deposit are more strongly and more complicatedly affected by tectonic thermal events than the surrounding rocks. This may also be one of the reasons why the independent tellurium deposit formed at the Dashuigou rather than in other areas.

The Eu/Sm ratio of quartz samples from the tourmaline-quartz vein at the host rock's bottom is 0.66 (Table 5), which is greater than the Eu/Sm values of almost all the rock types in Table 5, indicating that its origin is complex. Its parity ratio is 2.76, which is similar to that of the basalt, granite, and North American shale in Table 6, and also close to the average value of the crust, which further explains the complexity of its genesis. Its Sm/Nd ratio is 0.21. On the graph of Sm/Nd (Fig. 16), it not only falls within the Sm/Nd ratio range of Hawaiian alkaline basalts but also falls within that of the Middle-Lower Triassic metamorphic slate in this area. It shows that the formation of the tourmaline quartz vein has a certain connection to the basalt.

In general, the REEs of the Middle and Lower Triassic slates, marbles, and tourmaline quartz vein in the study area have the following characteristics: The total REE amount in the slate is relatively high, both the light and heavy REEs' fractionation is not obvious, and light REEs

Table 15 The logarithmic REE values of samples from the deposit's host rocks

Series #	Sample ID	La	Ce	Pr	Nd	Sm	Eu	Gd	Tb	Dy	Ho	Er	Tm	Yb	Lu
1	SL-05	2.00	1.77	1.73	1.62	1.36	1.15	1.20	1.13	0.97	0.91	0.85	0.37	0.80	0.79
2	SD-56	1.57	1.43	1.46	1.42	1.28	1.35	1.18	1.13	1.13	1.06	0.93	0.82	0.84	0.74
3	SL-11	− 0.27	− 0.31	− 0.49	− 0.73	− 0.92	− 0.69	− 1.01	− 1.00	− 1.01	− 1.26	− 1.48	− 1.22	− 1.50	− 1.19
4	SL-18	1.23	0.78	1.09	0.87	0.79	0.95	0.80	0.78	0.75	0.68	0.72	0.56	0.61	0.59
5	SD-49	0.45	0.22	0.26	0.11	− 0.10	− 0.16	− 0.21	− 0.18	0.20	− 0.32	− 0.51	− 0.48	− 0.52	− 0.49
6	SD-69	0.32	0.03	0.13	− 0.01	− 0.20	− 0.28	− 0.30	− 0.32	− 0.32	− 0.48	− 0.59	− 0.67	− 0.57	− 0.65
7	SL-03	1.90	1.68	1.64	1.51	1.28	1.09	1.12	1.15	1.00	0.94	0.92	0.88	0.88	0.81
8	SL-10	1.98	1.74	1.738	1.62	1.37	1.20	1.20	1.11	0.97	0.90	0.86	0.78	0.81	0.74
9	SL-01	1.78	1.58	1.54	1.40	1.16	1.15	0.93	0.90	0.90	0.86	0.85	0.84	0.89	0.85
10	SL-26	2.40	2.21	2.14	2.04	1.81	0.48	1.69	1.704	1.61	1.56	1.53	1.48	1.53	1.53
11	SL-22	2.43	2.22	2.15	2.04	1.74	1.19	1.57	1.53	1.35	1.28	1.25	1.19	1.22	1.22
12	SD-09	0.08	0.12	0.00	− 0.20	− 0.39	− 0.10	− 0.49	− 0.44	− 1.49	− 0.63	− 0.80	− 0.74	− 0.69	− 0.59
13	SD-65-1	1.54	1.48	1.58	1.58	1.52	1.17	1.38	1.38	1.36	1.32	1.26	1.13	1.14	1.12
14	SD-55-Py	0.00	− 0.08	− 0.09	− 0.21	− 0.21	− 0.31	− 0.44	− 0.30	− 0.24	− 0.42	− 0.56	− 0.56	− 0.47	− 0.45
15	SD-55-Pr	0.03	− 0.07	− 0.08	− 0.20	− 0.20	− 0.56	− 0.47	− 0.42	− 0.41	− 0.56	− 0.69	− 0.62	− 0.53	− 0.59
16	SD-57	0.70	0.70	0.79	0.60	0.60	0.78	0.39	0.44	0.34	0.26	0.10	0.13	0.28	0.32
17	SD-59	− 0.15	− 0.09	− 0.12	− 0.22	− 0.22	0.04	− 0.39	− 0.36	− 0.41	− 0.69	− 0.88	− 0.74	− 0.77	− 0.71

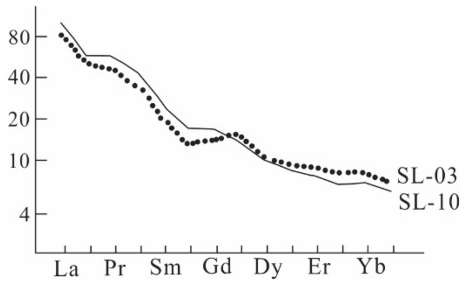

Fig. 14 Comparison of the chondrite-normalized REE models between the Upper Permian metabasalt and the Upper black section. (The sample numbers in the figure are consistent with those in Tables 3, 5, 9, 15)

are slightly more enriched than heavy REEs. On the chondrite-normalized REE diagram (Fig. 17), its curve is slightly right-dipping and it has small positive and negative europium anomalies, which are similar to the REE compositions of modern mid-ocean ridge tholeiite.

The total REE amount in marble is low, and the fractionation of light and heavy REEs is not obvious. On one hand, the cation of calcite is a six-coordinated mineral, which is generally related to the selective partition type of yttrium group REE. On the other hand, it is also related to thermal effect of the overlying basalt lava. Light REEs are slightly enriched, with weak positive europium anomalies or insignificant negative anomalies. Its chondrite- normalized REE model also forms a slightly right-dipping gentle curve, similar to that of its overlying slate.

The REE composition in the lower part of the deposit's host rocks' tourmaline quartz vein is characterized by a very low total REE amount (0.91×10^{-6}), an obvious

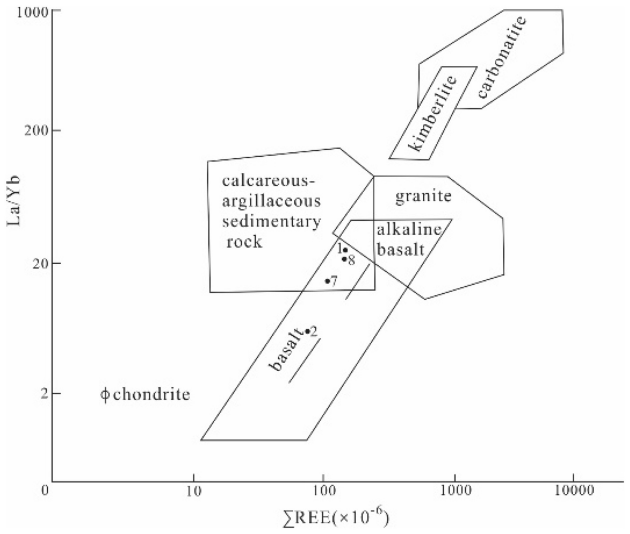

Fig. 15 The (La/Yb)-ΣREE plot of rock samples from the world. (The sample numbers in the figure are consistent with those in Tables 3, 5, 9 & 15)

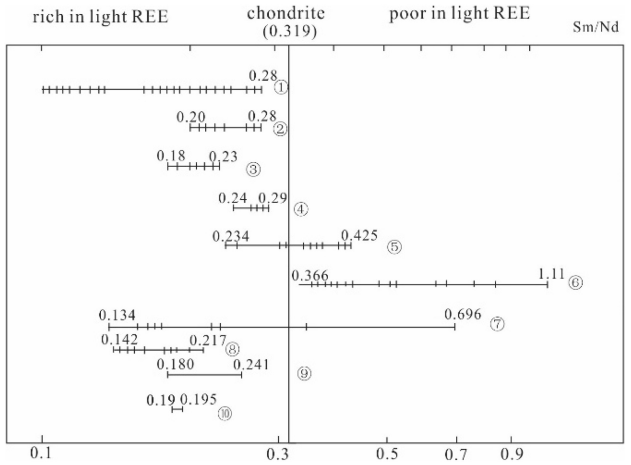

Fig. 16 Diagram of Sm/Nd ratios of different rock samples from the world (Richard et al. 1976). ①: alkaline basalt (Kimberley); ②: alkaline basalt (Grenada); ③: alkaline basalt (Hawaii); ④: tholeiite (Hawaii); ⑤: mid-ocean ridge basalt; ⑥: alpine peridotite (Alps); ⑦: xenolith in dipyridite; ⑧: sedimentary rock; ⑨: middle and lower Triassic slate from the deposit; ⑩: the upper Permian metabasalt and slate from the study area

positive europium anomaly (δEu = 1.88), poor fractionation of light and heavy REEs, and a slight enrichment of light REEs. Its REE distribution curve is slightly right-sloping.

In general, different rocks of the Middle and Lower Triassic in the study area have both differences and certain similarities in REE composition, indicating either that they have interacted with each other over their geological history or have a certain relationship in genesis. In addition, through the analysis of REE geochemistry, it can also be concluded that the Middle and Lower Triassic slates and the metamorphosed upper black rock member of the Upper Permian in this area all evolved from basalt magmas with complex origins, which to a certain extent proves that the Indosinian period tectonic–magmatic activity in the area was more intense, and the upper mantle material often upwelled into the crust.

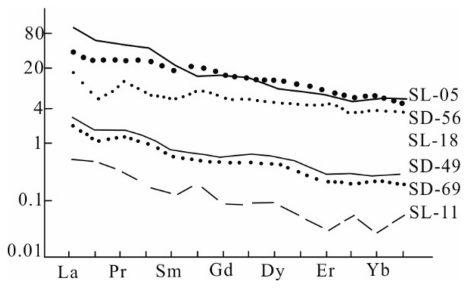

Fig. 17 The chondrite-normalized REE models of different rock samples from the Middle and Lower Triassic. (The sample numbers in the Fig. are consistent with those in Tables 3 & 5)

5.3 Geochemistry of silicon isotope

Silicon isotope geochemistry is a relatively new branch of stable isotope geochemistry (Ding et al. 1994). Relevant studies have shown that metamorphic rocks such as slate and schist can preserve the protolith's silicon isotopic composition during the metamorphic process. Accordingly, this paper attempts to restore the protolith of the deposit's metamorphic host rocks by using the host rock's silicon isotope. The silicon isotope results of three host rock samples and one quartz sample from the tourmaline-quartz vein are shown in Table 8.

According to Ding et al. (1994), the $\delta^{30}Si_{NBS\text{-}28}‰$ of intermediate-basic igneous rocks distribute between -1.0–0.3. The $\delta^{30}Si_{NBS\text{-}28}‰$ values of the three rock samples from the study area just fall into this range, indicating that their protolith is an intermediate-basic volcanic rock.

In addition, the $\delta^{30}Si_{NBS\text{-}28}‰$ of the two amphibole schist samples from the Qingchengzi lead–zinc deposit in Liaoning China are -0.1 and -0.3 respectively, while that of the plagioclase amphibole schist and amphibole schist from Gongchangling in Liaoning China are -0.1 and 0.1 respectively. All these rocks' protolith has been proven to be basalt. The $\delta^{30}Si_{NBS\text{-}28}‰$ of the deposit's schist and slate samples is also in the range of $-0.3 \sim 0.1$, again indicating that the protolith is basalt.

The $\delta^{30}Si_{NBS\text{-}28}‰$ of quartz samples from the tourmaline quartz vein in this area is -0.4, which should be within the $\delta^{30}Si_{NBS\text{-}28}‰$ range of granitoid rocks. According to Ding et al. (1994), the $\delta^{30}Si_{NBS\text{-}28}‰$ of granitoid rocks varies in the range of $-0.4 \sim 0.4$, with a peak value of -0.1 and an average value of -0.12.

6 Discussion

Combining the aforementioned host rock's geological, petrochemical, REE, and silicon isotope characteristics of the Middle and Lower Triassic metamorphic rocks in the study area, it can be seen that:

The deposit's hosts rock schist and slate are a set of regional low-temperature dynamic metamorphic rocks in the Indosinian period with low greenschist facies. The lithology and lithofacies change significantly, and the alteration intensity is different; the alteration within the deposit area is strong, and gradually weakens and disappears as it moves away from the deposit.

The host rock has undergone multiple geological tectonic movements, in which fault structures are developed and various alterations such as dolomitization, tourmalinization, muscovitization, silicification, sericitization, and chloritization are commonly seen in the region. In addition, pyrrhotite, lead–zinc, copper, pyrite, tellurium, bismuth, and gold-silver mineralizations are also very developed.

The protolith of the host rock, namely the schist and plate, is a set of basalt with complex genesis and composition. This set of basalts was formed under severe tectonic change and the upper mantle was in a severe non-equilibrium state.

The change of the marble's facies in the deposit is more obvious, indicating that the lithofacies and paleogeographical environment at the time of its formation were complex. Moreover, this set of marbles has been subjected to more than one tectonic thermal disturbance after its formation, resulting in anomalies in its geochemical characteristics, such as a certain degree of similarity between its REE composition and that of the overlying basalt. In addition, the black streaks in the banded marble are mainly composed of magnetite rather than carbonaceous argillaceous rocks. This is worthy of further study in the future.

Quantitative chemical analyses of Te, Bi, Se, As, Au, Ag, Cu, Pb, and Zn were conducted on different rock samples including granite dykes, metamorphic rocks, altered rocks, and carbonate veins of different geological times. The main findings are summarized below (Yin et al. 1994b, 1996b; Yin 1996a).

The Te content in the granites is under 1×10^{-7}, which is similar to its Clark value in the Earth's crust (Yin et al. 1995). Te in the metamorphic rocks is slightly higher than in the granites and varies slightly between metamorphic rocks of different geological times, while being relatively higher in the Triassic metamorphic rocks. Of the metamorphic rocks in the same geological time, the Te content in the slate and schist is higher than in the marble. Te content in rocks of the same stratohorizon of the same geological time also varies; namely, it is higher in rocks within the deposit than in those beyond the deposit. Te content is closely related to the alteration intensity; that is, the ore-forming elements are not derived from the country and/or host rocks, but instead from the mantle.

The numerous basalts of different geological ages developed in the area also indicate that this area is a very popular area for mantle materials to settle down. This proves from one side that the ore-forming elements of this deposit originate from the mantle.

The sulfur isotope results from the dominant ore mineral telluride in this deposit (Yin et al. 1994b, 1996a, b; Yin and Shi 2020), as well as results of fluid inclusions rich in Fe, Te, S, As, Bi, Se, H_2, CO_2, N2, and CH_4 etc. in the coexisting gangue minerals dolomite and quartz as well as ore mineral tellurides (Yin et al. 1994b, 1996a, b; Yin 1996a), all indicate that the ore-forming materials originate from the upper mantle.

Considering the widespread existence of mantle materials such as various basalts of different geological ages in

this area, it is reasonable that the deposit is formed by mantle-derived material richer in tellurium and bismuth elements, in the form of mantle plumes or hot spots, through the mantle degassing in the late Yanshanian orogeny (Yin et al. 1995). Its enrichment mechanism was these nanometer-level gaseous substances from the mantle enriched into ore bodies through the unique nano-effect, which was then brought into the crust to form the deposit.

7 Conclusions

Based on the discussions above, the authors reach the conclusions of this paper as follows:

Although they have been proposed by geological experts for many years, the above-mentioned petrochemical diagrams and eigenvalues are still of great practical significance for deciphering the protolith of many different kinds of metamorphic rocks.

These diagrams include but are not limited to the ACM, 100 mg-c-(al + alk), SiO_2-($Na_2O + K_2O$), (al + fm)-(c + alk) vs. si, (FeO + Fe_2O_3 + TiO)-Al_2O_3-MgO, c-mg, Al_2O_3-($Na_2O + K_2O$), the chondrite-normalized REE model, La/Yb-REE, and Sm/Nd ratio diagrams, etc. Additionally, these petrochemical eigenvalues include but are not limited to the molecular number, Niggli's value, REE parity ratio, CaO/Al_2O_3, $Fe^{3+}/(Fe^{3+} + Fe^{2+})$, the chondrite-normalized REE value, logarithmic REE value, various REE eigenvalues including Sc, Eu/Sm ratio, the total REE amount, light REEs, heavy REEs, δEu, Eu anomaly, Sm/Nd ratio, and Silicon isotope $\delta^{30}Si_{NBS\text{-}28}‰$, etc.

The existence of many basalts of different geological ages, as well as the existence of many intermediate-acid igneous rocks of different geological ages originating from these basic rocks, together with the existence of many lithospheric faults in the area, fully demonstrate that the formation of the Dashuigou tellurium deposit is closely related to the mantle degassing in the form of mantle plumes or hot spots. The gaseous materials discharged from the mantle are rich in nano-scale tellurium and bismuth and can be enriched through the nano-effect, which then rises to certain proper parts of the crust to form the deposit.

The ultimate power for the tellurium mineralization was from H_2 flow with giant energy, which was produced through radiation from the melted iron of the Earth's outer core. The H_2 flow results in the Earth's degassing, as well as the mantle and crust's uplift.

Acknowledgements Present research for this study was in part supported by Orient Resources Ltd. and College of Earth Sciences, Jilin University, Additional support was provided respectively by Prof. J. Zhou of Chinese Academy of Geological Sciences, and Prof. R. Pei of Chinese Academy of Geological Sciences, also an Academician of Chinese Academy of Engineering, both of whom provided insightful discussions and critical reviews of this manuscript. The measurements and chemical analyses, including the silicon and oxygen isotopes included in this article, were carried out in the labs of Chinese Academy of Geological Sciences in Beijing, China. The authors very much appreciate the time invested respectively by D.S. Yin, Mr. M. Storey, M.Eng. and P.Eng. with APEGBC of Canada, and J. Sparling, P.Geo. with APEGBC of Canada, for their review and editorial work on this contribution.

Author contributions The entire study included in the paper was proposed and organized by JY and SX, who should be regarded as co-first authors. Many of the figures and tables were prepared by YC and YY, who also helped the two co-first authors with the whole research. HS helped complete the chemical analyses of this study. All authors prepared and reviewed the manuscript and approved the final version. Conceptualization, JY; investigation, JY, SX, YC, YY, and HS; project administration, YC, YY and HS; writing—original draft, JY.

Data availability The data that support the findings of this study is available from the authors upon reasonable request.

Declarations

Conflict of interest On behalf of all authors, the corresponding author states that there is no conflict of interest.

References

Cao ZM, Luo, YN (1994) Mineral sequence and ore genesis of the Sichuan telluride lode deposit in China. In: New research progresses of the mineralogy, petrology and geochemistry in China. Lanzhou: Lanzhou University Publishing House, 476–478 (in Chinese)

Cao ZM, Wen CQ, Li BH (1995) Genesis of the Dashuigou tellurium deposit in Sichuan Province of China. Science China (b) 25(6):647–654 (**in Chinese with English abstract**)

Carmichael ISE, Turner FJ, Verhoogen J (1974) Igneous petrology. McGraw-Hill, Maidenhead

Chen YC, Mao JW, Luo YN, Wei JX, Cao ZM (1996) Geology and Geochemistry of the Dashuigou tellurium (gold) deposit in Western Sichuan, China. Atomic Energy Press, Beijing, 146pp (in Chinese with English abstract).

Chen YC, Yin JZ, Zhou JX (1994a) The first and only independent tellurium ore deposit in Dashuigou, Shimian County, Sichuan Province China. Sci Geol Sinica 3(1):109–113

Chen YC, Yin JZ, Zhou JX (1994b) Geology of the Dashuigou independent tellurium deposit of Sichuan Province. Acta Geosci Sin 29(2):165–167 (**in Chinese with English abstract**)

Ding TP, Jiang SY, Wan DF, Li YH, Li JC (1994) Silicon isotope geochemistry. Geological Publishing House, Beijing

Hu YZ, Deng J, Yuan N, He JP (1990) Stratigraphy and geochemistry of tin ore belt in northern Guangxi, China. Beijing Science and Technology Press, Beijing

Jensen LS (1976) A new cation plot for classifying subalkalic volcanic rocks: Ontario Ministry of Natural Resources Miscellaneous Paper 66, 22pp.

Leake BE (1964) The chemical distinction between ortho-and para-amphibolites. J Petrol 5(2):238–254

Li T (1976) Abundance of chemical elements in the Earth. Geochemistry 3:167–174 (**in Chinese**)

Liu YJ, Cao LM, Li ZL, Wang HN, Chu TQ, Zhang JR (1984) Element geochemistry. Science Press, Beijing

Luo YN, Cao ZM, Wen CQ (1996) Geology of the Dashuigou independent tellurium deposit. Southwest Communication University Publishing House, Chengdu

Luo YN, Fu DM, Zhou SD (1994) Genesis of the Dashuigou tellurium deposit in Sichuan Province of China. Bull Sichuan Geol 14(2):101–110 (**in Chinese with English abstract**)

Miyashiro A (1973) Metamorphism and metamorphic belts. Springer, Berlin

Niggli P (1954) Rocks and mineral deposits (Vol 1). WH Freeman, Boca Raton

Richard P, Shimizu N, Allègreab CJ (1976) $^{143}Nd/^{146}Nd$, a natural tracer: an application to oceanic basalts. Earth Planet Sci Lett 31(2):269–278. https://doi.org/10.1016/0012-821X(76)90219-3

Shen FQ (1985) Trace elements geochemistry of igneous rocks assemblage in Panxi rift. Sci Sinica 9:844–855

Simonen, A (1953) Stratigraphy and sedimentation of the svecofennidic, early Archean supracrustal rocks in southwestern Finland. Helsinki Government Press, Bulletin de la Commission géologique de Finlande, No 160, 64pp.

Wang RC, Lu JJ, Chen XM (2000) Genesis of the Dashuigou tellurium deposit in Sichuan Province, China. Bull Mineral Petrol Geochem 4:348–349 (**in Chinese**)

Winkler HGF (1979) Petrogenesis of metamorphic rocks. Springer, New York, NY,. https://doi.org/10.1007/978-1-4757-4215-2

Yin JZ (1996a) Paragenetic model and mineralizing mechanism of the Dashuigou independent tellurium deposit in Shimian County, Sichuan Province, China-the first and only independent tellurium deposit in the world. Chongqing Publishing House, Chongqing, 190pp (in Chinese with English abstract).

Yin JZ (1996b) The paragenetic model and mineralizing mechanism of the Dashuigou independent tellurium deposit in Shimian County, Sichuan - the first and only independent tellurium deposit in the world. Acta Geoscientia Sinica special issue, 93–97.

Yin JZ, Chen YC, Zhou JX (1994a) Mineralogical research of the Dashuigou independent tellurium deposit in Sichuan Province, China. Bull Mineral Petrol Geochem 3:153–155 (**in Chinese with English abstract**)

Yin JZ, Chen YC, Zhou JX (1995) K-Ar isotope evidence for age of the first and only independent tellurium deposit. Sci Bull 40(22):1933–1934

Yin JZ, Chen YC, Zhou JX (1996a) Geology and geochemistry of host rocks of the Dashuigou independent tellurium deposit in Sichuan Province, China. J Changchun Univ Earth Sci 26(3):322–326 (**in Chinese with English abstract**)

Yin JZ, Chen YC, Zhou JX (1996b) Geology and geochemistry of altered rocks of the Dashuigou independent tellurium deposit in Sichuan Province, China. J Xi'an Coll Geol 18(4):19–25 (**in Chinese with English abstract**)

Yin JZ, Shi HY (2019) Nano effect mineralization of rare elements–taking the Dashuigou tellurium deposit, Tibet Plateau, Southwest China as the example. Acad J Sci Res 7(11):635–642

Yin JZ, Shi HY (2020) Mineralogy and stable isotopes of tetradymite from the Dashuigou tellurium deposit, Tibet Plateau, southwest China. Sci Rep 10:4634

Yin JZ, Zhou JX, Yang BC (1994b) Geological characteristics of the Dashuigou tellurium deposit in Sichuan Province China. Earth Sci Front 1(4):241–243 (**in Chinese with English abstract**)

Yin JZ, Zhou JX, Yang BC (1994c) Rock-forming minerals and ore-forming minerals of the Dashuigou tellurium ore deposit unique in the world - a preliminary study. Sci Geol Sinica 3(2):197–210

Zhang QS (1984) Geology and metallogeny of the early Precambrian in China. Jilin People Press, Changchun